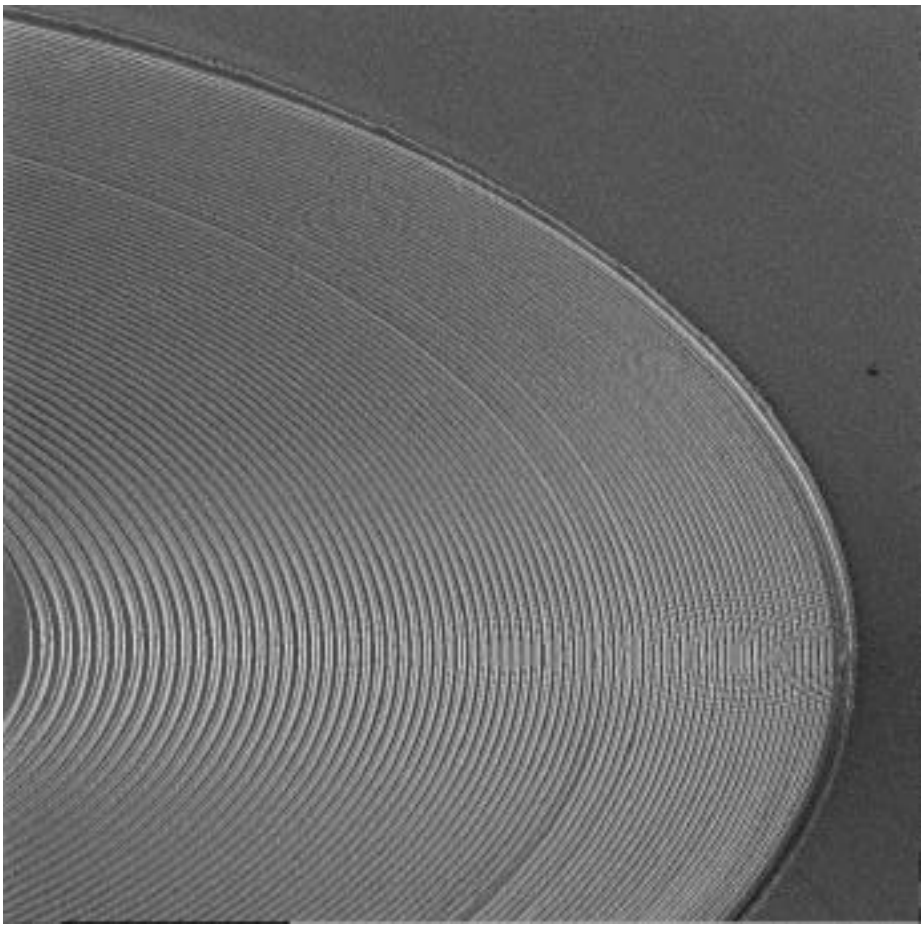

Fig. 2.33. Scanning electron micrograph of the TaSiN zone plate fabricated by FIB. The outermost zone width and thickness are 170 nm and 1.0 μm.

2.5 High-Energy X-ray Scattering

The SRI CAT high-energy program is part of the activities of the x-ray physics program. This program is based on the 1-ID beamline, which it shares with the other sector 1 programs. The activities of the high-energy program are divided into two main areas: optics development and experimental technique development.

The high-energy optics development effort has focused on developing monochromators that deliver high-quality x-ray beams in the energy range of 50-100 keV. We have based this program on several design goals:

- the x-ray beam should have both high brilliance and high flux,
- the monochromator should be tunable over a significant energy range,

- the monochromatic beam should be delivered to a separate experimental station, and
- no compromises should be made in the throughput of the monochromator due to inefficient cooling of the crystal optics.

To achieve these goals, we have built a high-energy double-crystal monochromator that uses the standard APS undulator. The first crystal of this monochromator is cryogenically cooled and, as a consequence, does not show significant thermal distortion when used with the undulator at fully closed gap. (It should be noted that, for maximum production of high-energy x-rays, a standard APS undulator needs to be operated at closed or nearly closed gap.) This is a significant achievement, because most (if not all) other high-energy beamlines use thick thermal filters to reduce the heat load on to their monochromators, which consequently reduces their throughput (particularly in the 50-65 keV range). One version of the high-energy monochromator, the double bent-Laue, is described below. We are currently working on a focusing configuration and a narrow-energy bandpass configuration.

The effort to develop high-energy experimental techniques is very diverse and has touched on several different scientific disciplines. One area of research utilizes the Kohzu double-crystal monochromator (the standard monochromator on beamline 1-ID) with Si (311) crystals to give an energy range of 25-45 keV. This has proved to be a very valuable energy range that is not accessible at most beamlines due to their use of mirrors. Experiments in this range are relatively straightforward extensions of lower energy techniques, but often the additional penetration from the higher energy x-rays makes a crucial difference. Two examples of such experiments are the polaron and confined-fluid studies discussed below.

Another area of research for high-energy techniques is experiments using x-rays above 50 keV (utilizing the high-energy monochromators described above). Most of the experiments at 1-ID in this energy range are geared toward using the penetration capabilities of high-energy x-rays. One example of this is powder diffraction from compounds with high-Z elements to reduce absorption corrections. Another example is the profiling of stress or phases in bulk parts. Much of this work is similar to neutron diffraction studies, but, with the high-energy x-rays, we are capable of obtaining much better spatial resolution. A third example is the ability to penetrate environmental chambers (e.g., furnaces). It is much easier to design furnaces for high-energy x-rays than for lower energies, and the resultant furnaces have superior performance (see below for one such device).

For future research, we will continue the research described above with additional emphasis in the optics development effort on focusing and in the technique development effort on stress/strain/texture measurements and in the *in situ* study of transient behavior of materials.

2.5.1 A New Bent-Crystal High-Throughput Monochromator

The standard double-crystal monochromator consisting of two flat, perfect crystals in a nondispersive setting is ideal for most low-energy experiments (below 30 keV) but is much less effective at high energies (above 60 keV). Flat perfect crystals do not extract and deliver high-energy photons from the white beam in an efficient manner due to the narrow Darwin widths of the crystals, the large value of the cotangent of the Bragg angle, and the increased opening angle of the undulator radiation at high energies where wiggler-like behavior sets in. An alternative monochromator optics design composed of two bent Laue crystals has been developed, which is considerably more efficient in extracting monochromatic high-energy synchrotron radiation. This monochromator delivers over ten times more flux onto a sample with the same energy bandpass as flat Bragg crystals in the 60-100 keV range. It has made 1-ID the only high-energy beamline in the world possessing the important features of high intensity, full tunablility, and phase-space (brilliance) preservation, while maintaining an in-line geometry.

The optics are shown schematically in Fig. 2.34. The white beam is incident on the first Laue crystal, cylindrically bent to a Rowland circle going through the source S1. The singly diffracted beam emerges as if emanating directly from a virtual source S2, also located on the first Rowland circle. The second crystal is also bent, but to a Rowland circle going through the virtual source S2. The doubly diffracted beam propagates as if coming from the virtual source S3 located on the second Rowland circle and close to the original source S1. The over ten-fold flux increase results from the bending strain-induced broadening of the crystal reflection's angular acceptance. Despite this broadening, one does not experience any significant increased energy bandpass because the curvature of the crystal is matched to the angular distribution of the white beam. This is characteristic of the Rowland geometry—all rays from any given point within the source impinge at the same angle onto the bent crystal lattice, leaving only a small source-size contribution.

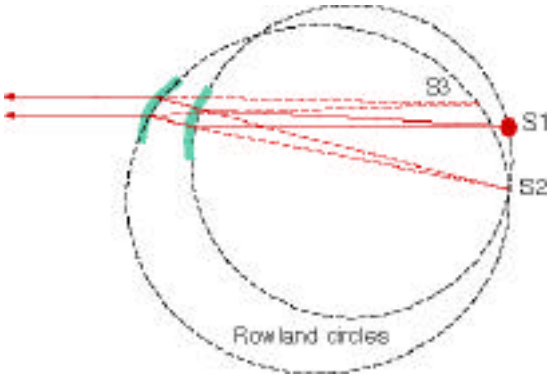

Fig. 2.34. Schematic of the high-energy, bent-Laue monochromator. S1 is the source of photons from the undulator, while S2 and S3 are virtual sources created by the crystal optics.

The technical challenge of implementing the bent double-Laue monochromator optics is achieving fine control and stability of the bend radii of the two crystals. The first crystal, in particular, poses additional difficulty due to the presence of the harsh conditions of closed undulator-gap heat load and cryogenic (liquid N_2) cooling. Crystal benders allowing excellent mechanical control and stability were developed, which operate by inducing the cylindrical bending deflection of a stiff triangular crystal by

pushing indirectly on its tip through a weak spring (see Fig. 2.35). This arrangement leaves the bend radii of the crystal insensitive to thermal or mechanical perturbations in the system. The cryogenic cooling for the first crystal is accomplished by flowing liquid N_2 through the copper blocks clamping the base of the crystal.

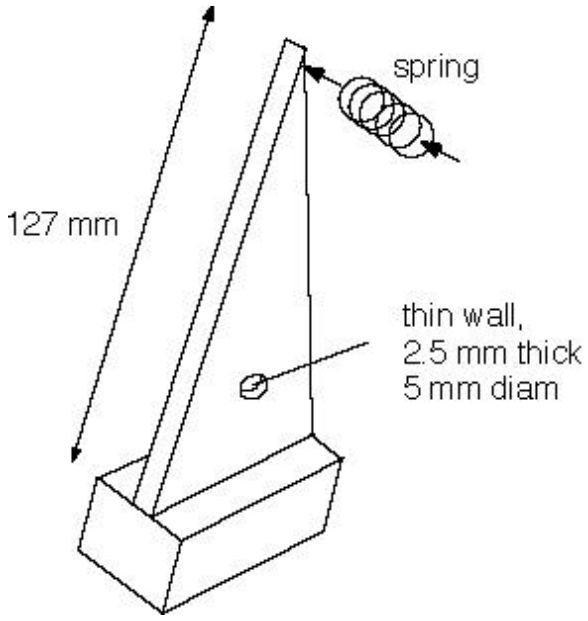

Fig. 2.35. Schematic of the mechanism to bend the Laue crystals for the high-energy monochromator.

2.5.2 High-Energy Applications

2.5.2.1 Polaron studies

The magnetic properties of the lanthanum manganese oxide class of materials have attracted tremendous interest recently because of the dramatic increase in conductivity these systems exhibit when the magnetic moments order ferromagnetically, either by lowering the temperature or by applying a magnetic field. This huge increase in the carrier mobility, which has been given the name "colossal magnetoresistance" (CMR), is of both scientific and technological interest. In particular, it is anticipated that these materials may provide the next generation of read/write heads for the magnetic data storage industry, while the "half-metallic" behavior provides fully spin-polarized electrons for use in magnetoelectronics applications and for sensors in a variety of applications, such as in the automotive industry.

Colossal magnetoresistance can be strongly enhanced in systems with reduced dimensionality, and so there has been considerable interest in the two-layer Ruddlesden-Popper compounds, $La_{2-2x}Sr_{1+2x}Mn_2O_7$. The reduced dimensionality leads to significant extension of the temperature range over which magnetic correlations are important and thereby allows a detailed examination of the link between local spin correlations and the resulting magnetotransport. One of the central questions in the field of manganites concerns the lattice involvement in the mechanism of CMR. While the relation between ferromagnetism and conductivity was explained in terms of double exchange, it is now clear that a full understanding of these materials must include the lattice degrees of freedom. In particular, the formation of lattice polarons above the Curie temperature has been inferred from a variety of measurements, but direct evidence has been lacking.

The measurements were performed on a single crystal of the double-layer compound $La_{1.2}Sr_{1.8}Mn_2O_7$, cleaved from a boule that was grown using the floating zone technique. The x-ray data were taken on the

1-ID-C diffractometer, mostly using a high-energy beam of 36 keV to provide enough penetration in transmission geometry. Additional measurements were taken in reflection geometry with 21 keV. A wide range of reciprocal space was explored, including the (*h*0*l*) and (*hhl*) planes. The crystal structure of $La_{1.2}Sr_{1.8}Mn_2O_7$ is body-centered tetragonal (space group *I*4/*mmm*) with *a* 3.87 Å and *c* 20.15 Å, and consists of MnO_2 bilayers separated by (La, Sr) sheets. Previous neutron scattering measurements (Osborn et al., 1998) have evidenced two-dimensional ferromagnetic correlations that peak in intensity at the combined metal-insulator and Curie transition at T_C = 112 K and extend over a large temperature range above T_C.

Our measurements (Vasiliu-Doloc et al., 1999) have revealed charge localization in the paramagnetic-insulating phase of the layered $La_{1.2}Sr_{1.8}Mn_2O_7$ CMR material, with the associated diffuse polaron scattering that originates from the lattice distortions around the localized charges.

Figure 2.36(a) shows a contour plot of the diffuse x-ray scattering in the [*h*, 0, *l*] plane around the (2, 0, 0) reflection. Only the $l > 0$ half is shown, but the pattern is symmetric with respect to $l = 0$. The sharp rod of scattering along the [0, 0, *l*] direction is resolution limited in the [*h*, *k*, 0] plane and is associated with stacking faults. The *h*-scans across the diffuse scattering at *l*=0.5 shown in Fig. 2.36(b) clearly indicate that this diffuse scattering is anisotropic and strongly temperature dependent, with a dramatic response at T_C.

Part of this diffuse scattering is due to acoustic phonons, but the sudden change at T_C cannot be due to conventional acoustic phonons, as confirmed by inelastic neutron measurements. A good description of the **q**-dependence of this diffuse scattering has been obtained in terms of Huang scattering, consistent with a Jahn-Teller type distortion around the Mn^{3+} ions.

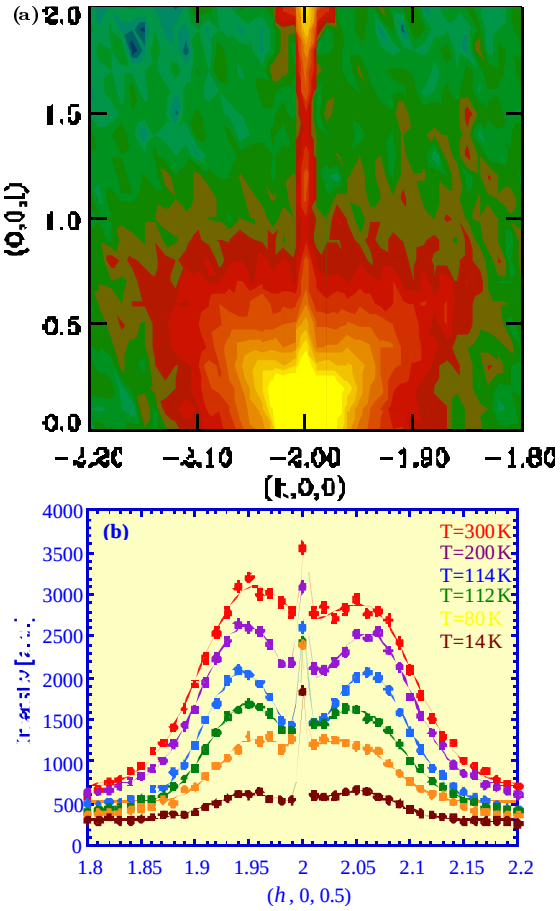

Fig. 2.36. (a) Contour plot showing the lobe-shaped pattern of x-ray diffuse scattering around (2, 0, 0). (b) X-ray h-scans across the diffuse scattering at l = 0.5 at a series of temperatures.

The measurements also reveal the presence of broad incommensurate peaks in the paramagnetic phase, as shown by the contour plot of the x-ray intensity at 125 K in the (*hk*) plane at l = 18 in Fig. 2.37(a). These peaks are characterized by a wave vector (±ε, 0, ±1) as measured from the nearest fundamental Bragg peak, where ε 0.3 [in terms of reciprocal lattice units (2π/*a*, 0, 2π/*c*)]. The in-plane incommensurability is evident in the x-ray *h*-scans shown in Fig. 2.37(b) at different temperatures. Note that this peak increases and then rapidly decreases in intensity as we cool through T_C. Figure 2.37(c) shows that the temperature dependence of the incommensurate peak intensity is remarkably similar to the Huang scattering derived from the x-ray scattering by subtracting the estimated thermal diffuse scattering. This indicates that both types of scattering are associated with the development of polarons above T_C. The incommensurate peak intensity falls slightly more rapidly than the Huang scattering with increasing temperature. This is consistent with ascribing the Huang scattering to individual polarons and the incommensurate peaks to polaron correlations, which become stronger with decreasing temperature. Below T_C we observe a "melting" of the polaron correlations occurring simultaneously with the collapse of the polarons themselves. These results have been confirmed using neutron scattering at the National Institute of Standards and Technology (NIST) Center for Neutron Research and provide important new insights into the relation of polarons to colossal magnetoresistance.

Charge and orbital ordering have been observed at low temperature in a number of insulating, antiferromagnetic cubic manganites at small and large ($x \geq 0.5$) doping,

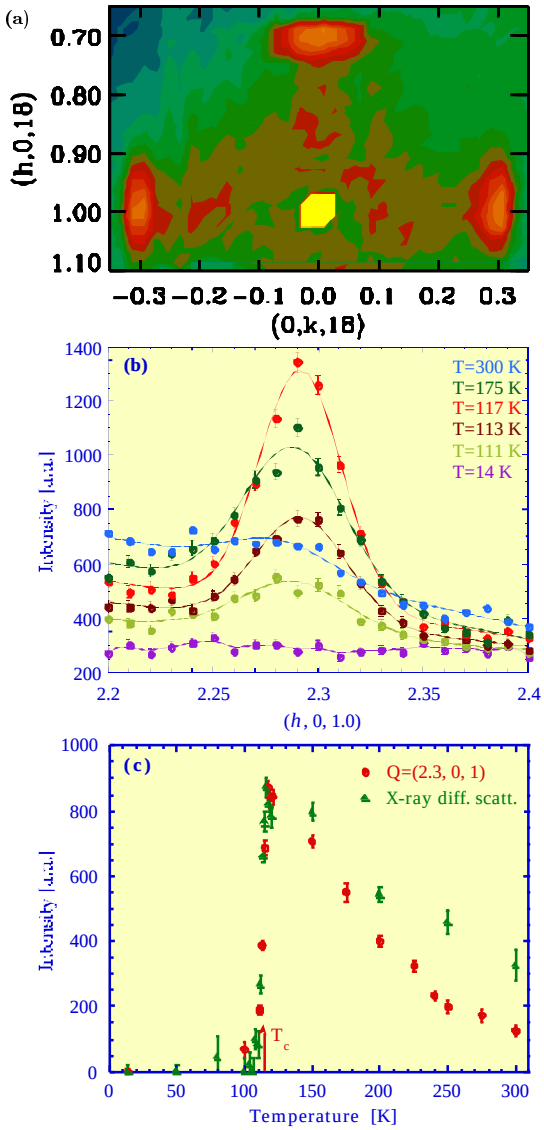

Fig. 2.37. (a) Contour plot of the x-ray intensity in the (hk) plane at l = 18, collected at T=125 K. Three incommensurate peaks due to polaron ordering are observed, characterized by the wave vector (±ε, 0, l) or (0, ±ε, l). The expected fourth peak was not accessible experimentally. (b) X-ray h-scans through the incommensurate peak (2.3, 0, 1) at different temperatures. The higher scattering at small h is due to the proximity of the lobe-shaped diffuse scattering around the Bragg peak. (c) Temperature dependence of the x-ray intensity of the (2.3, 0, 1) incommensurate peak (red closed circles), and of the diffuse scattering after correction for the phonon contribution (green closed triangles).

as well as in layered manganites with x = 0.5. However, short-range charge ordering in the paramagnetic phase of an optimally

doped CMR ferromagnet is a novel feature observed here. In the present x=0.4 system, the charge correlations are not strong enough to win the competition with the double-exchange interaction, and the charges delocalize at the ferromagnetic transition, where the charge peaks collapse and the lattice strain relaxes. It is the delicate balance between double exchange, Coulomb repulsion and the lattice strain field that dictates whether the material is a ferromagnetic metal or charge-ordered insulator at low temperatures.

2.5.2.2 Confined fluids

Fluids confined between solid surfaces have been of great interest to researchers over the last few years (Granick, 1999). This is because the structural and other properties of such fluids differ considerably from bulk fluids at the same temperature, and this has implications for our basic understanding of phenomena such as lubrication, adhesion, surface chemistry, etc. Surface force apparatus (SFA) measurements (Bhushan et al., 1995; Demirel and Granick, 1996) and computer simulation studies (Thompson et al., 1992; Gao et al., 1995; Gao et al., 1997) have found evidence for layering of the liquid molecules in liquid films confined to thicknesses of a few molecular diameters, but direct structural evidence has been lacking. [Evidence for layering near a bulk liquid/solid interface has however recently been obtained from x-ray reflectivity (Yu et al., 1999).]

X-ray reflectivity provides the most direct method for probing the structure of liquid films in the direction normal to the confining surfaces. However, such experiments on films confined at thicknesses of a few nanometers present significant challenges, such as: (a) penetration of the beam through the confining walls and minimization of the scattering from the walls (for which extremely small and high-energy x-ray beams are essential), and (b) alignment of two solid surfaces to a controllable parallel separation of nano-meters over square millimeters of area (for which the surfaces must be both highly polished and flat over such length scales, as well as dust-free). In addition, the layering is rapidly destroyed by surface roughness, which typically should not exceed ~ 0.3 nm. We have utilized specially designed silicon substrates (Fig. 2.38) having a diameter of

(a)

(b)

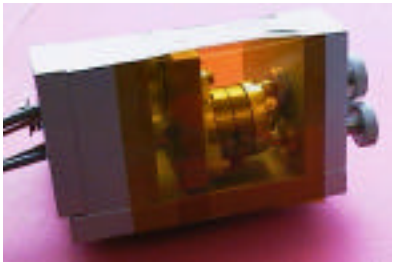

Fig. 2.38. Components of the experimental setup for x-ray scattering on confined liquids. (a) Specially designed silicon substrates (25.4 mm diameter). The area of confinement is the bridge in the center. (b) The sample cell.

1 inch (25.4 mm), an rms roughness of 3 Å (determined by x-ray scattering) and a convex curvature with a height variation of less than 100 Å over the whole sample area (determined by interferometry). Two grooves were etched in each surface, which left a bridge of the size (2 x 4) mm^2 in the center part. The bridge is the area of confinement with a resulting height variation of less than 10 Å. For the experiment, the liquid was spread over the surface of one substrate in a class 1 clean-room. Both substrates were put together so that the grooves formed tunnels that were the paths for the x-rays to the area of confinement (Fig. 2.38). The gap distance between both silicon pieces was controlled by piezodrivers.

The x-ray reflectivity experiments were performed at the SRI-CAT beamlines. The characteristics of the setup were checked at station 2-BM-B where liquid hexadecane ($C_{16}H_{34}$) was used. Some reflectivity measurements taken at 30 keV photon energy are depicted in Fig. 2.39. They show that the gap size shrinks linearly with increasing pressure of the piezodevices. A minimum gap size of 74 nm was achieved, but no evidence was found for layering.

Further reflectivity measurements using octamethylcyclotetrasiloxane (OMCTS) were performed at station 1-ID-C, again with a photon energy of 30 keV (Fig. 2.40).

We were able to achieve 10 times higher pressure compared to the run at 2-BM-B and thus could get much smaller gap distances. Also the flux was much higher so that more details of the reflectivity would be seen.

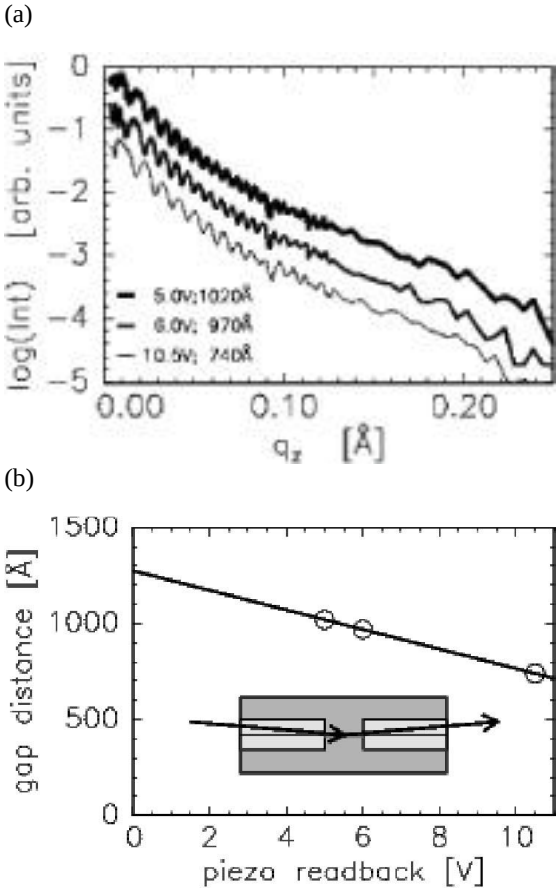

Fig. 2.39. Gap measurements of the confined liquid setup. (a) Some reflectivity measurements at different readbacks of the piezodrivers. They show oscillations due to the gap size. (b) Characteristics of the piezodrivers and a sketch of the sample with the area of confinement in the center.

The reflectivity curves from OMCTS have been fit using the following model: The silicon substrates and native oxide layers were represented with the appropriate step functions of electron density normal to the surface suitably smeared to take into account ~ 0.3 nm roughness and obtained by fitting to the reflectivity of the bare substrates. The OMCTS liquid between the substrates was modeled by a series of Gaussian peaks representing in-plane averaged electron densities of the molecular layers. Extremely

good fits were obtained in this manner (Fig. 2.41). We found that both the gap and the number of molecular layers decreased in a quantized fashion with increasing pressure, from a gap size of 25.2 Å containing three

close-packed layers to a gap size of 19.9 Å at the highest pressures, containing 2 non-close-packed-layers. The width of the Gaussian peaks corresponded rather well to the size of the OMCTS molecule (diameter ~ 8 Å).

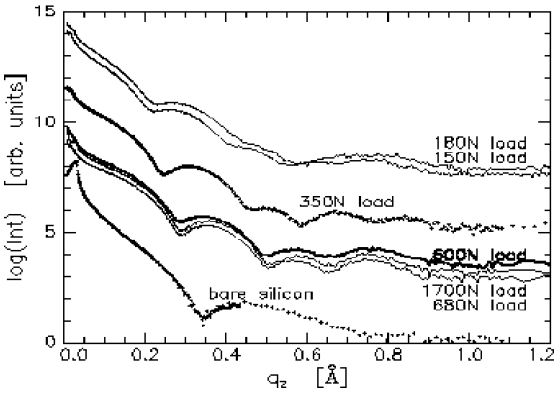

Fig. 2.40. Reflectivities on confined OMCTS. Different pressures have been applied on the silicon substrates. Essentially, only three different reflectivities can be seen.

2.5.2.3 High-temperature powder diffraction

Furnace development

Often conventional x-ray powder diffraction employing flat-plate sample geometry has surface roughness and absorption problems. The corrections for these effects are complicated and some times produce erroneous results. These corrections are eliminated by the use of transmission geometry, which is possible through the use of high-energy x-rays. Other advantages for using high-energy x-rays for powder diffraction include the ability to penetrate through environmental chambers (e.g., high-temperature furnaces) and the ability to gather data far out into reciprocal space.

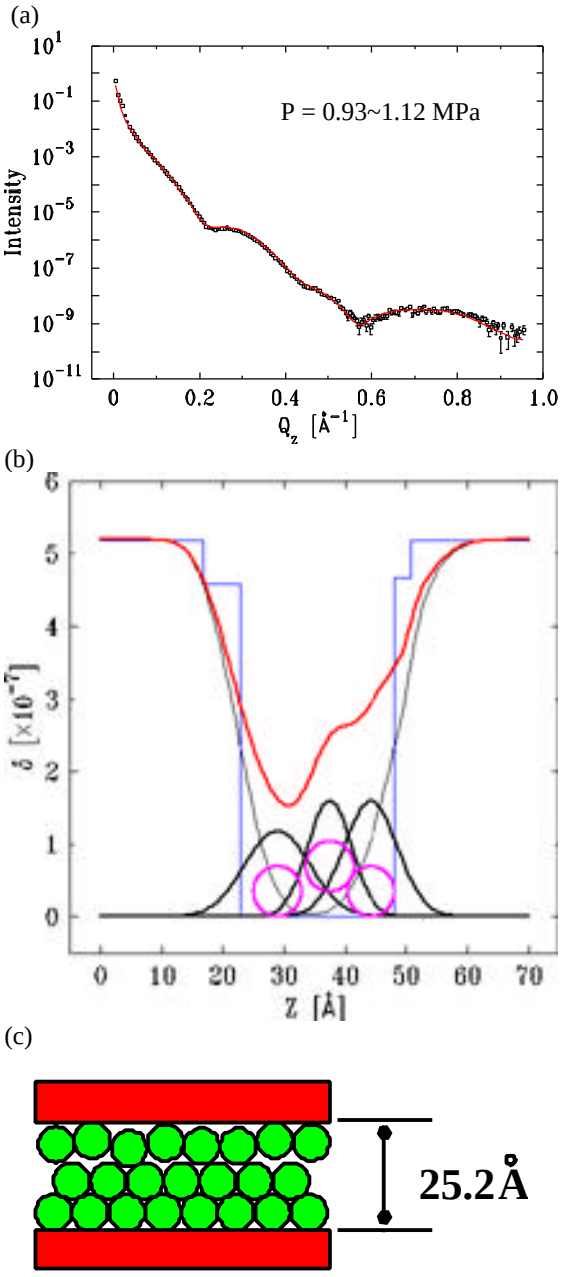

Fig. 2.41. (a) Measured and modeled reflectivity for pressures between 0.93 and 1.12 MPa. Fitted curve uses the electron density model shown in (b). This model is schematically represented in (c).

Temperature control is the most important issue for the high-temperature powder diffraction experiments. A uniform temperature applied on the entire sample volume is a critical requirement for the design of high-temperature furnaces. In collaboration with a group from Ames Laboratory, a high-energy furnace (up to 1500°C) has been designed (Fig. 2.42) specifically for use with high-energy x-rays employing transmission diffraction geometry (Margulies et al., 1999). This allows for full bulk sampling, low thermal gradients (<1°C/mm), and precise control of the sample environment. Unlike the flat-plate geometry, the transmission geometry allows the solid-liquid, as well as solid-solid, phase transitions to be studied. For example, in a study of the phase transition of α− to β–TiRh, high-quality time-resolved data was obtained at 60 keV (Fig. 2.43). There is disagreement in the literature as to whether this phase transition is first or second order. The data clearly show the coexistence of both phases over a narrow temperature range.

We are continuously developing improved versions of the furnace that can reach even higher temperatures with easier alignment and are exploring research projects that can utilize the capability of the high-temperature powder-diffraction technique.

Clathrate thermoelectric materials

There is considerable interest in developing new materials for thermoelectric applications that might allow the replacement of current refrigeration technology with efficient, all-solid-state

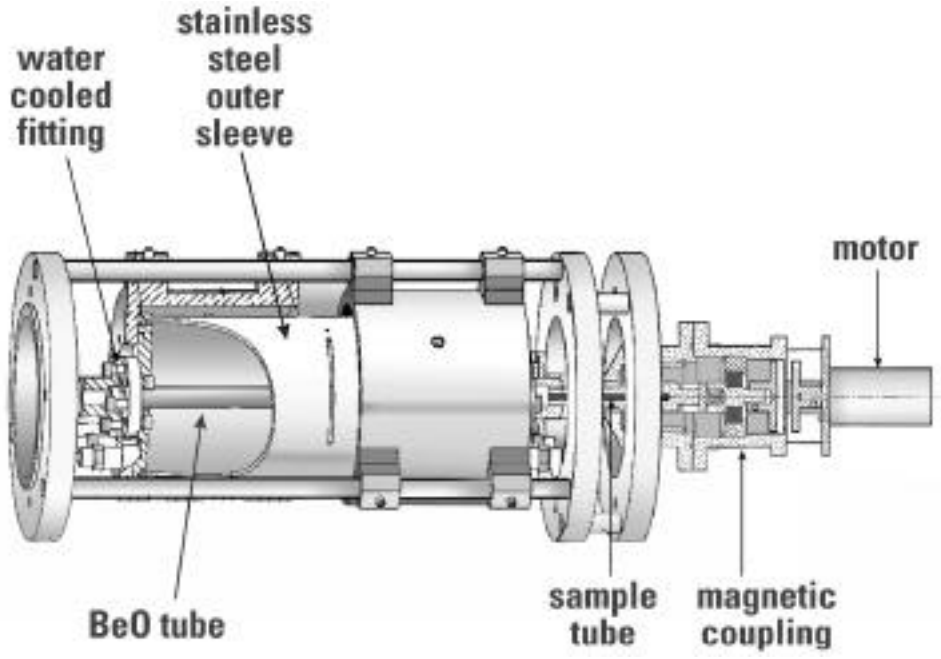

Fig. 2.42. Schematic of the furnace used in the time-resolved studies.

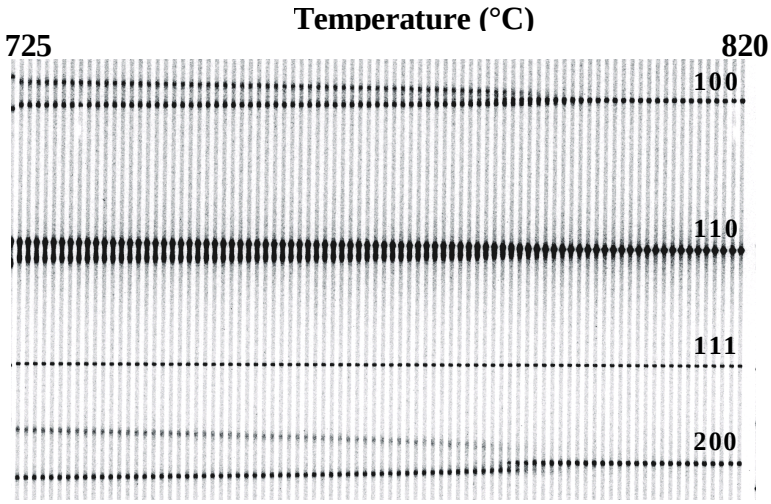

Fig. 2.43. A section of image plate showing the tetragonal to cubic phase transition in TiRh, area of transition. The stripes are individual "snap-shots" taken every 8 seconds.

devices. Semiconductors with a clathrate structure are attractive candidate thermo-electric materials. They consist of 3D frameworks of covalently bonded Si, Ge or Sn, with species, such as Cs, Rb, K, Na, Sr, or Eu, rattling inside cavities in the framework. The frameworks are typically heavily doped and can be constructed from face-sharing polyhedra of various types and sizes (see Fig. 2.44 for an example structure).

The disorder associated with the vibrational motion of species inside the framework cavities and any disorder introduced by doping the framework can have a profound impact on the thermoelectric properties of these materials. The rattling of species in the cavities ("cages") reduces the material's thermal conductivity and the distribution of dopant ("guest" atoms) over the available framework sites influences the electronic structure of the materials. A more complete understanding of the disorder induced by the guest atoms inside their oversized cages would not only lead to a better understanding of the transport properties but may also enable one to predict transport properties from a structural analysis. Therefore, accurate structure analysis is a vital part of this research project.

For this kind of analysis, a few important criteria for the powder-diffraction data are: high-order reflections, minimal absorption corrections, and good signal-to-background ratios (especially at high orders). Employing high-energy x-rays allows the collection of high-order reflections and reduces absorp-tion effects, especially if some of the guest atoms are high-Z elements.

In collaboration with A. P. Wilkinson and R. A. Young from Georgia Institute of Technology, S. B. Schujman and G. A. Slack from Rensselaer Polytechnic Institute, and G. S. Nolas from Marlow Industrial Inc., we have examined $Cs_8Na_{16}Ge_{136}$,

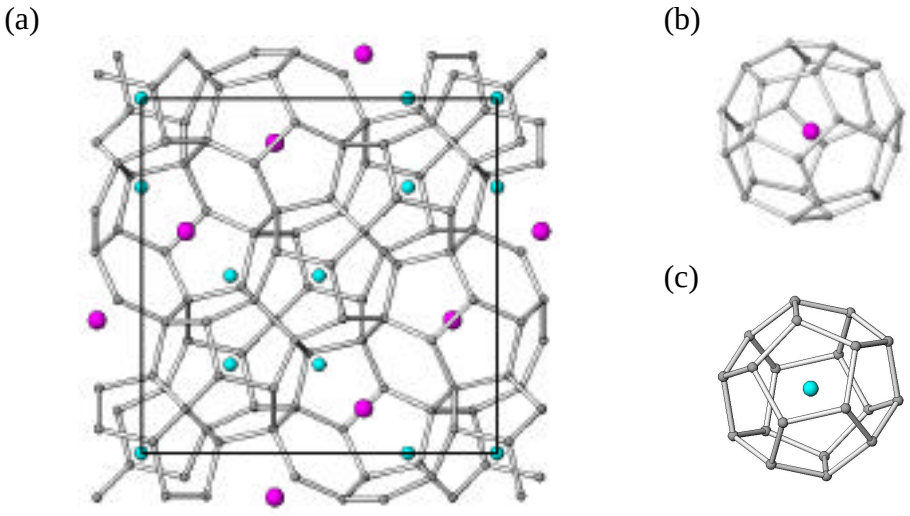

Fig. 2.44. The type II clathrate structure (a) adopted by $Cs_8Na_{16}Ge_{136}$ and its relatives can be constructed from face sharing (b) hexakaidecahedra and (c) dodecahedra.

$Eu_8Ga_{16}Ge_{30}$ and $Cs_8Cd_4Sn_{42}$. Powder diffraction data were acquired for the first two samples using 80 keV photons at temperatures of 20, 150 and 298 K. Data were obtained on the $Cs_8Cd_4Sn_{42}$ sample at 298 K using 80 keV photons and at wavelengths just below the Sn and Cd K-edges, respectively. In addition, a 20 K data set was obtained using a wavelength just below the Cd K-edge.

$Cs_8Na_{16}Ge_{136}$

In this material, Cs and Na occupy the hexakaidecahedral and dodecahedral cavities, respectively. The atomic displacement parameters (ADPs) for the Cs and Na indicate that they are heavily disordered at room temperature. However, on cooling to 20 K, the disorder associated with the Cs site disappears, but the Na still shows signs of disorder. Presumably this residual disorder is static in origin with the true location of the sodium being slightly displaced from the center of the dodecahedral cavity. The general quality of the fits to the diffraction data is good (Fig. 2.45), but the residual static disorder on the sodium site could not be modeled due to the relatively low x-ray scattering power of the sodium. A comparison of the ADPs obtained

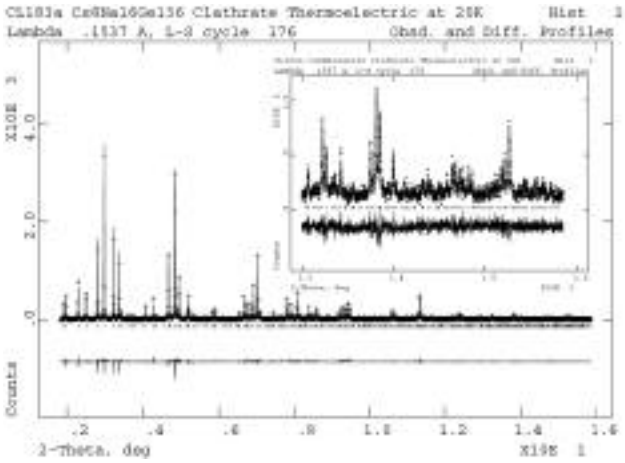

Fig. 2.45. A Rietveld fit to the data obtained on $Cs_8Na_{16}Ge_{136}$ at 20 K using 80 keV x-rays. Usable data were obtained out to ~16° 2θ, corresponding to a minimum d-spacing of around 0.55 Å (see inset).

from the powder diffraction data with those obtained from single-crystal data collected at temperatures above 100 K showed excellent agreement for the heavy atoms in the structure (Cs and Ge).

$Eu_8Ga_{16}Ge_{30}$

This material adopts a type-I clathrate structure with the europium completely occupying two different types of cages. A random distribution of the gallium and germanium over the three crystallographically distinct framework sites was assumed during the data analyses, as there was insufficient scattering contrast between the Ga and Ge to explore the possibility of dopant ordering. The ADPs for both Eu sites indicated considerable disorder at 298 K. At 20 K, the ADPs for one of the two distinct Eu sites showed very strong evidence for static disorder. As the europium scatters very strongly and data to relatively high Q were available, it was possible to model the disorder using four statistically occupied positions displaced from the cavity center. The use of a split site model gave significantly better agreement with the data than a simple model with a large ADP.

$Cs_8Cd_4Sn_{42}$

The structure analysis for this material was performed using a combination of the 80 keV, Cd K- and Sn K-edge data that had been collected at 298 K. The Cd and Sn K-edge data sets were both collected close to the bottoms of the corresponding edges to minimize absorption effects. The data analysis indicated that the cadmium predominantly occupies only one of the three available framework sites. The fit to the 20 K data set was of very high quality and clearly indicated that there was little disorder of the Cs at this temperature, suggesting that the disorder of the Cs observed at 298 K was dynamic and not static. Additionally, the ADPs for the framework atoms supported the conclusion that the cadmium was confined to one of the available framework sites.

Other high-energy x-ray research

In addition to the work mentioned above, we have conducted several other high-energy powder-diffraction experiments on beamline 1-ID with outside user groups. These groups include Argyriou and coworkers (Argonne Materials Science Division); Gray and coworkers (Griffith Univ., Brisbane, Australia); and Kramer and coworkers (Ames Lab./Iowa St. Univ.). Measurements on liquids and amorphous materials have been made with Price, Saboungi, and coworkers (Argonne Materials Science Division); Billenge, Petkov, and coworkers (Michigan St. Univ.); and Zwanziger and coworkers (Indiana Univ.). High-energy stress/strain experiments have been conducted with Noyan (IBM) and Ustundag (Cal. Tech.); Pyzalla (Hahn-Meitner Inst., Berlin); Gnaupel-Herold (NIST, Gaithersburg); Winholtz (U. of Missouri-Columbia); and Varma and coworkers (Los Alamos National Laboratory).